ARTICLES

Journal of Semiconductors
(2022) 43, 052201
doi: 10.1088/1674-4926/43/5/052201

Tin dioxide buffer layer-assisted efficiency and stability of wide-bandgap inverted perovskite solar cells

Bingbing Chen[1, 2, 3, 4, ‡], Pengyang Wang[1, 2, 3, 4, ‡], Ningyu Ren[1, 2, 3, 4, 5], Renjie Li[1, 2, 3, 4], Ying Zhao[1, 2, 3, 4], and Xiaodan Zhang[1, 2, 3, 4, †]

[1]Institute of Photoelectronic Thin Film Devices and Technology, Renewable Energy Conversion and Storage Center, Solar Energy Conversion Center, Nankai University, Tianjin 300350, China

[2]Key Laboratory of Photoelectronic Thin Film Devices and Technology of Tianjin, Tianjin 300350, China

[3]Engineering Research Center of Thin Film Photoelectronic Technology of Ministry of Education, Tianjin 300350, China

[4]Collaborative Innovation Center of Chemical Science and Engineering (Tianjin), Tianjin 300072, China

[5]School of Physical Science and Technology, Inner Mongolia University, Key Laboratory of Semiconductor, Hohhot 010021, China

Abstract: Inverted perovskite solar cells (IPSCs) have attracted tremendous research interest in recent years due to their applications in perovskite/silicon tandem solar cells. However, further performance improvements and long-term stability issues are the main obstacles that deeply hinder the development of devices. Herein, we demonstrate a facile atomic layer deposition (ALD) processed tin dioxide (SnO_2) as an additional buffer layer for efficient and stable wide-bandgap IPSCs. The additional buffer layer increases the shunt resistance and reduces the reverse current saturation density, resulting in the enhancement of efficiency from 19.23% to 21.13%. The target device with a bandgap of 1.63 eV obtains open-circuit voltage of 1.19 V, short circuit current density of 21.86 mA/cm^2, and fill factor of 81.07%. More importantly, the compact and stable SnO_2 film invests the IPSCs with superhydrophobicity, thus significantly enhancing the moisture resistance. Eventually, the target device can maintain 90% of its initial efficiency after 600 h storage in ambient conditions with relative humidity of 20%–40% without encapsulation. The ALD-processed SnO_2 provides a promising way to boost the efficiency and stability of IPSCs, and a great potential for perovskite-based tandem solar cells in the near future.

Key words: atomic layer deposition; tin dioxide; additional buffer layer; efficiency and stability; inverted perovskite solar cells

Citation: B B Chen, P Y Wang, N Y Ren, R J Li, Y Zhao, and X D Zhang, Tin dioxide buffer layer-assisted efficiency and stability of wide-bandgap inverted perovskite solar cells[J]. *J. Semicond.*, 2022, 43(5), 052201. https://doi.org/10.1088/1674-4926/43/5/052201

1. Introduction

Recently, a record power conversion efficiency (PCE) of perovskite/silicon monolithic tandem solar cells has increased to 29.8%[1], which has broken the theoretical efficiency of a single junction silicon cells. With rapid progress in increasing PCE, perovskite/silicon tandem devices have become an inventive competitor in the photovoltaic performance race[2–4]. Even though the single-junction perovskite device with N–I–P architecture presented power conversion efficiencies (PCEs) of 25.5%, in tandem devices the highest performance was obtained with inverted perovskite solar cells (IPSCs)[5–7]. Therefore, surmounting the performance loss and instability issues of inverted perovskite devices are extremely important to accelerate the commercialization of perovskite/silicon tandem technology[8].

Up to now, the PCE of IPSCs has reached to 23.37% with a certificate efficiency of 22.75%[9], which was the highest value reported for IPVSCs. Compared with the normal N–I–P type PSCs, the large open-circuit voltage (V_{OC}) deficit is considered as one of the main obstacles, particularly in wide bandgap IPSCs, which slows its performance development[10, 11]. Actually, plenty of research has been done for suppressing the V_{OC} loss in IPSCs. These mainly include components regulation[12–14], crystallization control[15–17], bulk or surface defect passivation[11, 18–23] and energy level alignment[24–27]. Due to the easy solution coating process, the good physical and electronic contacts with the perovskite layer and the favorable passivation functionality, [6,6]-phenyl-C61-butyric acid methyl ester (PCBM) is one of the popular materials for the electron transport layer in IPSCs[28–30]. However, the direct contact between PCBM and the top metal electrode will lead to serious non-radiative recombination, thus resulting in the failing collection of charge carriers to the cathode. Bathocuproine (BCP) is the most common material used in IPSCs to block hole transport and facilitate electron collection[9, 18, 28–32]. Nevertheless, this insulating layer needs to be sufficiently thin to allow electron tunneling. In general, solution-processed perovskites have a rough surface, which makes the thickness of the insulator layer difficult to control. Therefore, a buffer layer that can achieve uniform coverage on the rough perovskite surface is the most pressing need for highly efficient IPSCs.

Besides the PCE, the main challenge for actual commercialization in PSCs lies instability[33–35]. The electron transport lay-

Bingbing Chen and Pengyang Wang contributed equally to this work.
Correspondence to: X D Zhang, xdzhang@nankai.edu.cn
Received 4 DECEMBER 2021; Revised 20 DECEMBER 2021.

ers (ETLs) play a more important role in IPSCs towards stable devices. Through rational design, the ETL can provide a self-encapsulating function. For instance, You *et al.* employed solution-processed zinc oxide (ZnO) nanoparticles as electron transport layers, comparing with devices with organic charge transport layers, which showed ~90% retention of its initial PCE after 60 days storage in ambient[36]. Fang *et al.* designed a PCBM/cerium oxide (CeO_x) nanocrystal bilayer structure with good long-term stability under ambient air storage[37]. Tin dioxide (SnO_2) with high electron mobility and a well band alignment with the perovskite absorption layer, which is a superior material in single-junction planar PSCs or highly efficient perovskite/silicon tandem solar cells[38–40]. Zhu *et al.* exploited the solution-processed SnO_2 nanocrystals (NCs) to act as efficient ETLs in the IPSCs, a PCE of 18.8% with remarkable ambient stability was obtained[41]. Raninga *et al.* used atmospheric pressure chemical vapor deposition (CVD) to achieve a pinhole-free and conformal SnO_2 layer, and thus protect the perovskite against mechanical and environmental destruction, resulting in a PCE of 19.4% in an IPSCs[42].

Here, SnO_2 using the atomic layer deposition (ALD) method was designed as an additional buffer layer on the BCP layer for improving efficiency and stability in wide bandgap IPSCs. Compared with previous methods, ultra-thin and compact SnO_2 could be obtained by ALD process. Moreover, vacuum conditions and suitable for large area fabrication also make it great potential for future commercialization. It was found that SnO_2 layer was homogeneously coated on the sample surface eliminating the possible leakage current and thus raising the shunt resistance (R_{sh}) and reducing the reverse current (J_0). Finally, 21.13% efficiency was obtained in the wide-bandgap (1.63 eV) inverted perovskite device with a SnO_2 additional buffer layer. Moreover, ALD growing SnO_2 layer with a great compactness which enhanced the moisture contact angle and improved stability of the perovskite device.

2. Experimental section

2.1. Device fabrication

ITO substrates were cleaned by detergent, DI water, acetone and isopropanol for 30 min, respectively. Then the substrates were treated by UV-ozone for 20 min. And then, PTAA (5 mg/mL in CB) solution was spin-coated onto the substrates at 5000 rpm for 30 s and annealed at 100 °C for 10 min in the glovebox with nitrogen condition. 1.5 M PbI_2 : $PbBr_2$ (83 : 17) precursor solution was spin-coated onto PTAA at the speed of 3000 rpm for 30 s and annealed at 70 °C for 1 min. And then, a mixture solution of organic salt (FAI : MABr : MACl = 90 : 6 : 9) was spin-coated onto the film at a speed of 3500 rpm for 30 s followed by annealing at 150 °C for 20 min in ambient air (30%–40% humidity). The passivation layer GABr (3 mg/mL in IPA) was fabricated by spin-coating at 5000 rpm for 30 s followed by annealing at 100 °C for 5 min. Subsequently, PCBM solution (20 mg/mL in CB) was spin-coated onto the perovskite film at a speed of 1500 rpm for 30 s. BCP solution (0.5 mg/mL in IPA) was spin-coated onto the PCBM film at a speed of 5000 rpm for 30 s. And then, the devices were moved into ALD devices to deposit SnO_2 film with different thicknesses. The deposition of the SnO_2 with the following processing sequence: 0.5 s TDMASn pulse, 15 s purge (20 sccm N_2), 0.1 s deionized water pulse, and 15 s purge (20 sccm N_2) at 85 °C. Finally, 150 nm of Cu top electrode were thermally evaporated under vacuum with a shadow mask. The area of the cells is 0.12 cm^2, when measuring, a 0.0887 cm^2 mask was used to define the accurate aperture area for the cells.

2.2. Material and device characterizations

2.2.1. Materials

Lead bromide ($PbBr_2$), chlorobenzene (CB), dimethylsulfoxide (DMSO), N, N-dimethylformamide (DMF) and isopropyl alcohol (IPA) were purchased from Sigma-Aldrich. Polybis (4-phenyl) (2,4, 6-trimethyl-phenyl) amine (PTAA), [6,6]-Phenyl C61 butyric acid methyl ester (PCBM), bathocuproine (BCP), lead iodide (PbI_2), bromide guanidine (GABr), formamidinium iodide (FAI), methylammonium bromide (MABr), and methylammonium chloride (MACl) were purchased from Xi'an Polymer Light Technology Corp.

2.2.2. Device characterizations

Scanning electron microscopy (SEM, FEI NanoSEM650) was used to characterize the morphology of the SnO_2 films and also the cross-sectional image of the fully device. The current density–voltage (*J*–*V*) characteristics of the devices were measured by Keithley 2400 Source meter under AM 1.5G illumination with Xenon-lamp based solar simulator (Enli. Tec., Taiwan). The intensity of the light was calibrated with KG-5 filter Si photodiode. And the area of the solar cells was 0.08875 cm^2. When measuring the device performance, a metal mask was used to reduce the influence of the scattered light. The forward scan (0–1.2 V, scan rate 20 mV/s, delay time 20 ms) and reverse scan (1.2–0 V, scan rate 20 mV/s, delay time 20 ms) were applied. External quantum efficiency (EQE) spectra were conducted by Enli Tec (Taiwan) measurement system in the wavelength from 300 to 900 nm with a scanning step of 10 nm. The photoluminescence (PL) and time-resolved photoluminescence (TRPL) spectroscopies were measured with a laser wavelength of 475 nm and power of 0.2 mW (Edinburgh FS5). The root mean square (RMS) roughness of different films was taken from atomic force microscopy (AFM) images measured with ARTCAM-130-SIINT (ARTRAY Co. Ltd., Japan).

3. Results and discussion

Firstly, SnO_2 with different thickness as an additional buffer layer is designed. Fig. 1(a) presents the illustration of the IPSCs devices with a structure of ITO/PTAA/Perovskite/PCBM/BCP/SnO_2/Cu. The thickness of perovskite film is around 550 nm (Fig. S1). Current density–voltage (*J*–*V*) curves of the devices with SnO_2 films of different thicknesses (0, 10, 20, 30, 40 nm) are shown in Fig. 1(b). The results demonstrate that the devices with SnO_2 layer obtain a higher V_{OC} and fill factor (FF), short-circuit current density (J_{SC}) is also slightly increased. The control device without SnO_2 layer achieves a PCE of 17.47%. When the thickness of SnO_2 film increased from 10–30 nm, the PCE is enhanced to 17.60, 18.29 and 20.02, respectively. While the thickness of SnO_2 increased to 40 nm, the performance of IPSCs decreased to 19.82%, which may be due to the thick SnO_2 film introducing a high series resistance. The performance of IPSCs with dif-

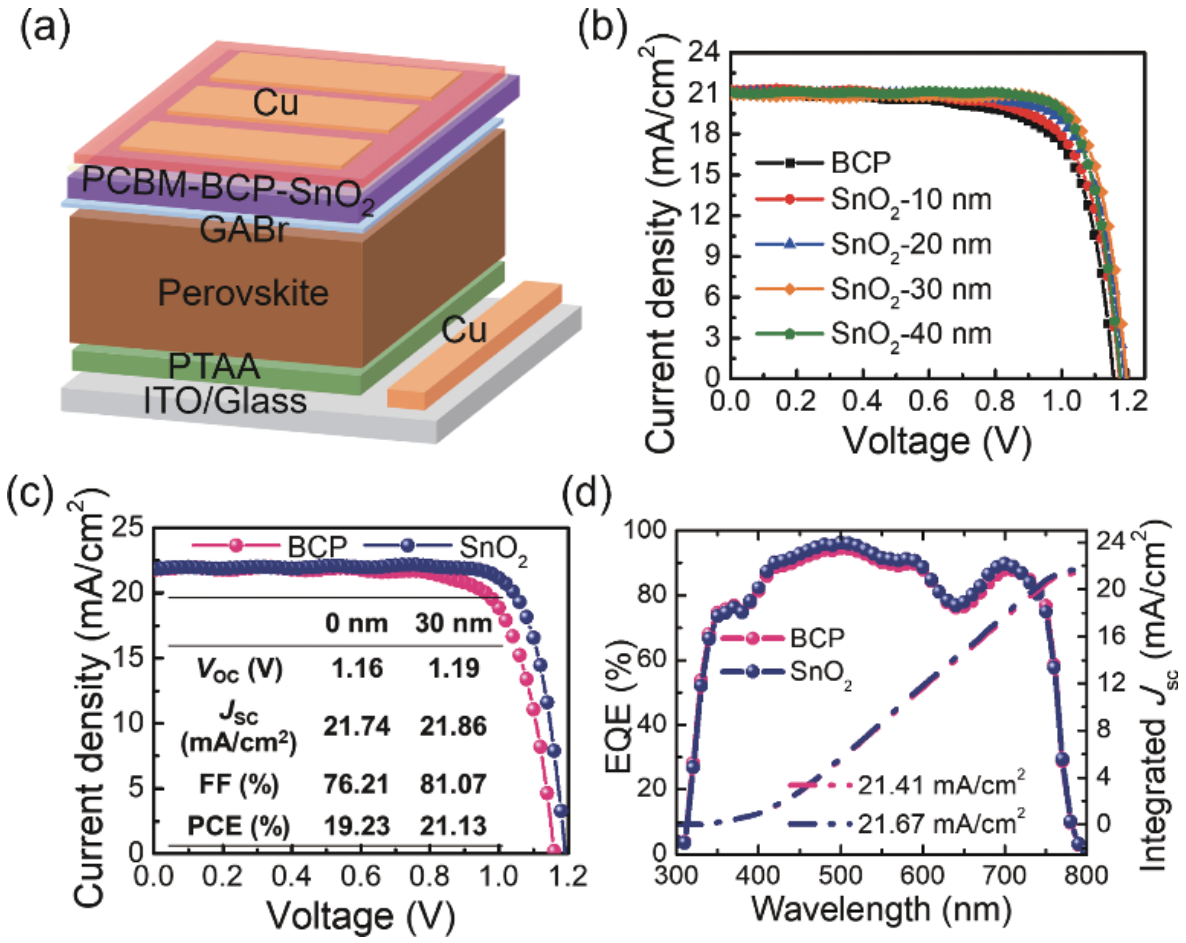

Fig. 1. (Color online) Device structure and performance with different SnO_2 thickness. (a) The architecture of the device in this work. (b) *J*–*V* curves with different SnO_2 thickness. (c, d) The champion devices *J*–*V* and EQE curves with 30 nm SnO_2 buffer layer, respectively.

ferent scanning directions are presented in Fig. S2 and Table S1. And the statistical diagrams of the device performances are shown in Fig. S3. After optimization, the device of 30 nm SnO_2 exhibited champion performance with a V_{OC} of 1.19 V, J_{SC} of 21.86 mA/cm^2, FF of 81.07%, and the corresponding PCE of 21.13%. While, the control device only with a PCE of 19.23%.

J–*V* and external quantum efficiency (EQE) curves are presented in Figs. 1(c) and 1(d), respectively. The integral current densities of the devices are 21.41 and 21.67 mA/cm^2 which are well matched with the J_{SC} in *J*–*V* measurement. The bandgap of the perovskite can be determined by the tangent of the curve to the base line which is also presented. The ultraviolet-visible absorption of perovskite material and $(ahv)^2$ versus energy of perovskite film are shown in Fig. S4. It can be found that the bandgap of the perovskite is about 1.63 eV. Therefore, the V_{OC} deficit (E_g/q–V_{OC}) is only of 440 mV. This value is a lower V_{OC} loss which compares to other wide bandgap IPSCs as present in Table S2. Moreover, device performance of different SnO_2 thicknesses with or without BCP are also investigated (Fig. S5). BCP is essential when a thinner SnO_2 is deposited. With increasing the thickness of SnO_2, the role of BCP is gradually diminished. Devices with BCP and a suitable thicker SnO_2 buffer layer achieved a higher FF and PCE.

Time-resolved photoluminescence (TRPL) is employed to investigate the transport and recombination dynamics of photoinduced carriers in perovskite films without and with 30 nm SnO_2 buffer layer (Fig. 2(a)). The biexponential function is applied to fit the TRPL decay curves (Eq. (1))[43]:

$$Y = A_1 e^{-t/\tau_1} + A_2 e^{-t/\tau_2} + y_0, \quad (1)$$

where τ_1 and τ_2 are the lifetimes for the carrier transport and recombination, and A_1 and A_2 are the corresponding amplitudes. τ_1 is due to the carrier transport occurring in the surface of the perovskite film, whereas τ_2 could be attributed to the bulk and surface recombination. The devices without SnO_2 obtained τ_1 = 42.01 ns and τ_2 = 146.43 ns, respectively. While τ_1 = 37.65 ns and τ_2 = 181.59 ns are given with SnO_2. The decrease of τ_1 indicates faster electron transfer from perovskite to ETL with the presence of SnO_2. The increased τ_2 indicates a slower recombination rate. The film with defferent thickness of SnO_2 film were also presented in Fig. S6, and the fitting value of the carrier transport and recombination lifetime were shown in Table S3. The results illustrate that perovskite film with SnO_2 additional layer achieves a faster carrier extraction and a lower carrier quenching between the active layer and the transport layer, which is a good agreement with the higher FF and V_{OC}. R_{sh} of the devices without or with 30 nm SnO_2 are also calculated (Fig. 2(b)). The higher R_{sh} benefits the enhancement of the FF, which further confirms the excellent function of the SnO_2 buffer layer.

Fig. 2(c) shows the dark *J*–*V* curves of the devices without and with a 30 nm SnO_2 buffer layer. According to the Schottky junction model, diode ideality factor (n) and J_0 can

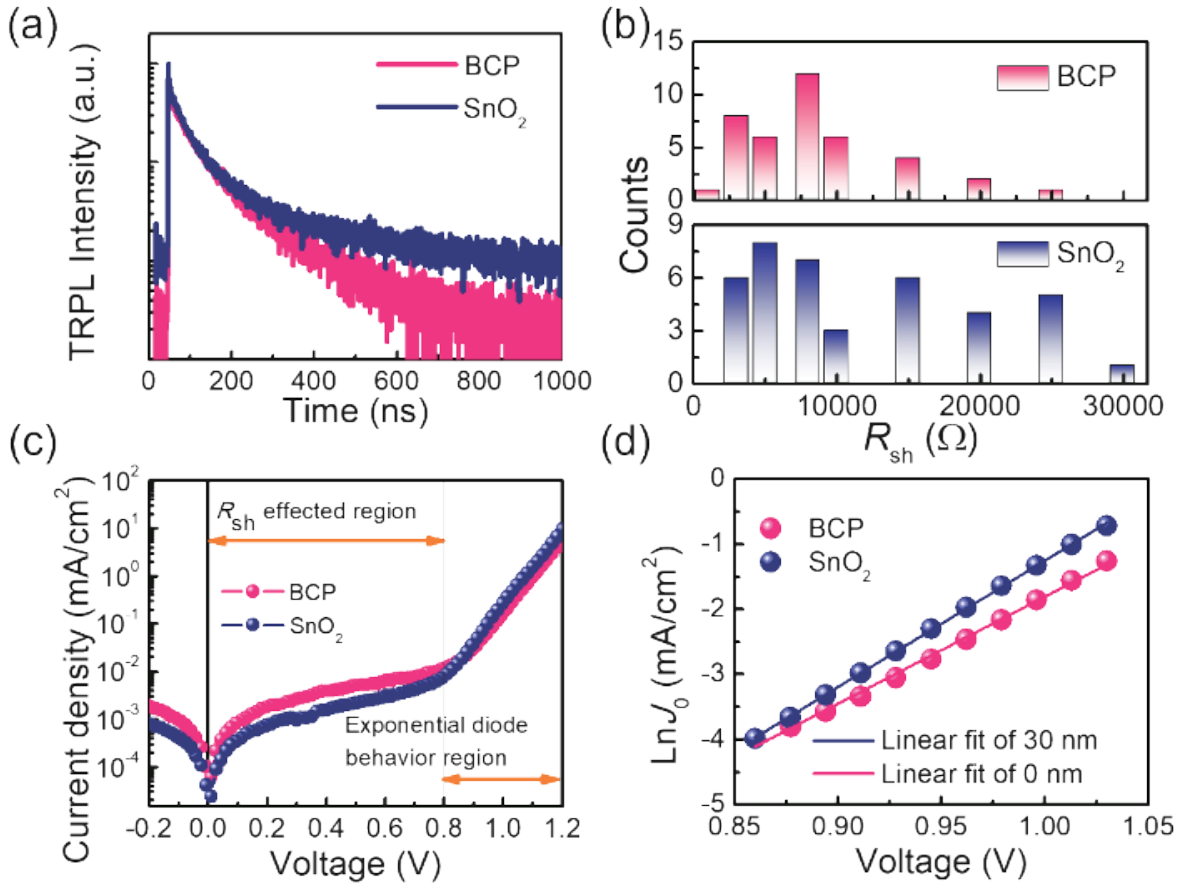

Fig. 2. (Color online) Device performance without the SnO_2 buffer layer and with 30 nm SnO_2 buffer layer. (a) TRPL curves of the devices. (b) R_{sh} of the devices. (c) *J*–*V* curves of the devices under dark condition. (d) Fitting curves for calculation the n and J_0 from the dark *J*–*V* data.

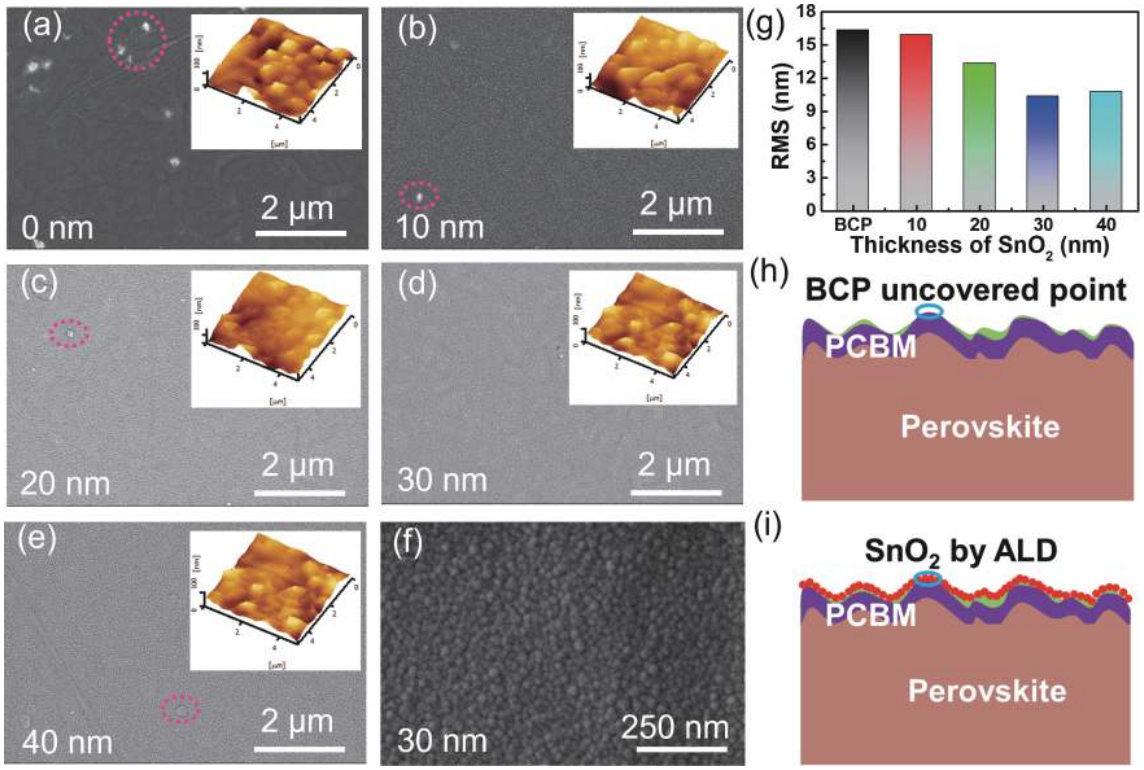

Fig. 3. (Color online) Top view SEM of SnO_2 layer with various thicknesses based on the structure of ITO/PTAA/Perovskite/PCBM. (a), (b), (c), (d) and (e) with thickness of SnO_2 of 0, 10, 20, 30 and 40 nm, respectively. (f) With a larger magnification to show a clearer morphology of SnO_2 with the thickness of 30 nm. (g) RMS of the films with different thicknesses of SnO_2. (h) The schematic diagram of the sample with a thinner BCP layer. (i) The schematic diagram of the sample with a BCP and SnO_2 bilayer.

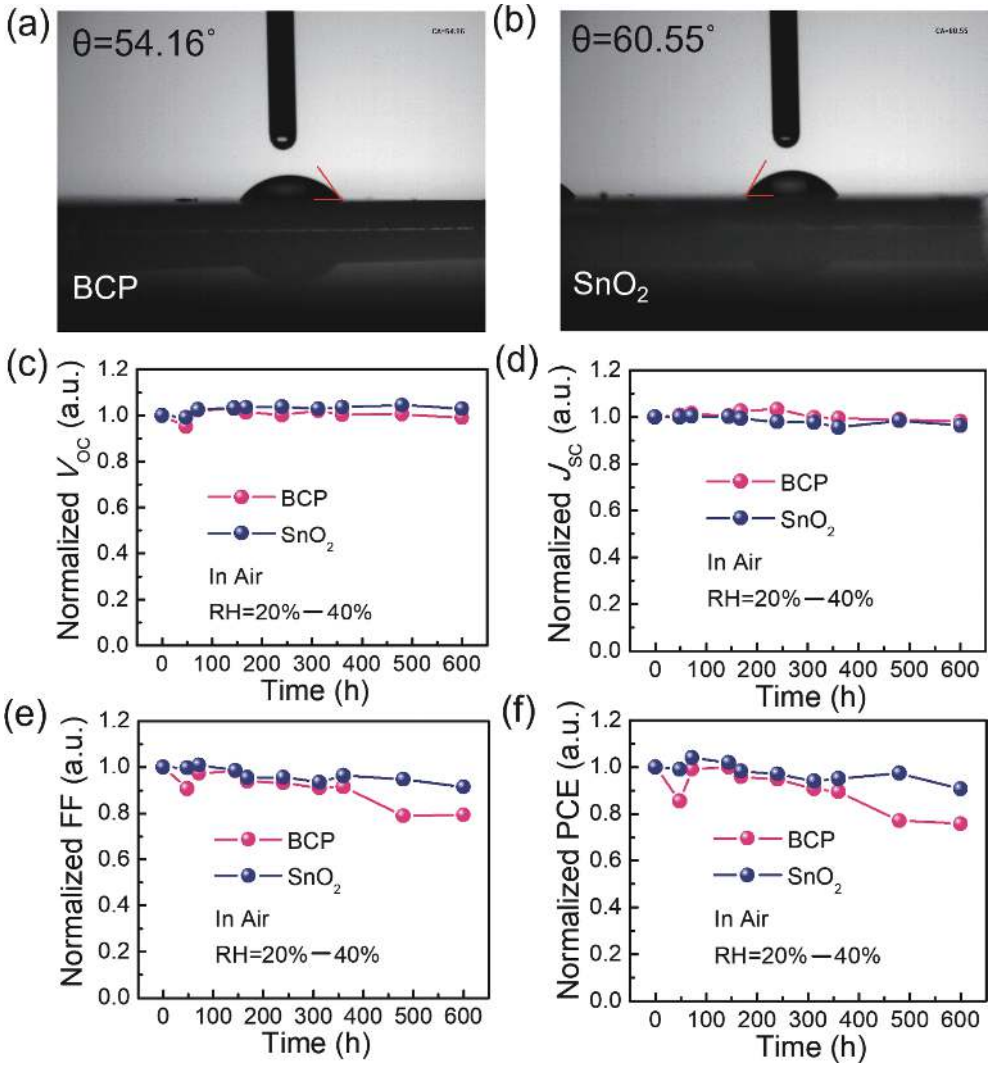

Fig. 4. (Color online) (a, b) The water contact angle of the device without and with SnO_2. (c–f) Normalized V_{OC}, J_{SC}, FF and PCE of perovskite devices without and with 30 nm SnO_2 kept in the atmosphere (25 °C, 20–40 RH%) without encapsulation for 600 h, respectively.

be obtained by fitting the linear *J*–*V* curve (exponential diode behavior region) as shown in Fig. 2(d). The Eq. (2) shows in the following[44]:

$$J = J_0\left[\exp\left(\frac{eV}{nkT} - 1\right)\right], \tag{2}$$

where *J* is the current density value, *V* is the applied voltage, *T* is the absolute temperature, *k* is the Boltzmann constant, *e* is the electron charge. From the equation we can find that *n* and J_0 are close related with the slope and intercept of the linear fitting of $\ln(J_0)$ versus *V*. The control device has a slope of 16.41, while the device with 30 nm SnO_2 film has a slope of 19.38. The larger the slope, the smaller the *n,* which proved a better diode characteristic. The corresponding J_0 values of 1.10×10^{-9} and 1.22×10^{-8} mA/cm^2 are obtained of the devices with and without SnO_2 film. The results clearly indicated that device with SnO_2 film has a lower J_0, which means a smaller leakage current, resulting in a higher V_{OC}.

A top-view scanning electron microscope (SEM) is primordially verified to show the surface morphology of the devices with or without SnO_2 (Fig. 3). Figs. 3(a)–3(e) were the SnO_2 film morphologies with the thickness of 0, 10, 20, 30 and 40 nm on the structure of glass/ITO/PTAA/perovskite/PCBM/BCP, respectively. As expected, SnO_2 films with different thicknessness demonstrate different coverage, and the surface becomes increasingly compact as the thickness increases. SnO_2 with 10 nm obtains the poorest coverage while all of the devices with thickness over 20 nm show uniform and dense morphology, and the device with 30 nm SnO_2 has the best coverage. Fig. 3(f) shows a clearer morphology of SnO_2 with the thickness of 30 nm, and it further illustrates that the compact SnO_2 layer can uniform coverage of the ETL layer, obstructing the immediate contact with the metal electrode. And the illustrations present the corresponding surface morphology of the films with different thicknesses of SnO_2 by an atomic force microscope (AFM). The root-mean-square (RMS) roughness of the films is shown in Fig. 3(g), SnO_2 film deposited by ALD can effectively reduce surface roughness. The assumed schematic diagrams of the performance improvement are demonstrated in Figs. 3(h) and 3(i). Perovskites with a rough surface, so the solution method BCP with a thinner thickness may not cover the PCBM completely. This supplies an opportunity of direct contact between PCBM and metal electrode, causing a non-radiative recombination center and reducing the R_{sh}, and thus degrading the performance of the

devices. Whereas, the ALD method SnO_2 can conformal growth on the uneven surface which completely prevents the current leakage. That more distinctly illustrates the reason of the increased V_{OC} and FF of the devices with SnO_2 additional buffer layers.

The water contact angles are presented in Figs. 4(a) and 4(b). It is evidently shown that the film with a 30 nm SnO_2 layer has a larger contact angle which can better resistance to moisture and then stabilize the device. The devices without and with 30 nm SnO_2 are stored in a glove box with nitrogen (N_2) condition (Fig. S7). Both of the devices show relatively high stability, the device performance with SnO_2 is basically keeping the same efficiency without decay after 600 h. Figs. 4(c)–4(e) show the normalized V_{OC}, J_{SC} and FF of the device with and without SnO_2 layer in the air atmosphere with relative humidity between 20%–40% without encapsulation, respectively. Fig. 4(f) presents the normalized PCE of the devices with or without SnO_2 layer. It is clearly shown that the device with SnO_2 still maintains 90% of initial efficiency after 600 h. Nevertheless, the efficiency of the device without SnO_2 drops down to less than its 70%. We can find that the attenuation of the PCE is mainly due to the decrease of FF and V_{OC}, while the J_{SC} are barely changed. Fig. S8 presents the changes of series resistance (R_s) for the two devices, we supposed the increased R_s is the reason for the FF and V_{OC} losses.

4. Conclusions

In summary, we have demonstrated that the ALD-processed SnO_2 as an additional buffer layer in IPSCs is a general approach to enhance the device's performance and stability. The results show that this additional buffer layer can significantly increase the R_{sh} and reduce the leakage current, thus enhancing the FF and V_{OC}. Meanwhile, the uniform SnO_2 film with good hydrophobicity to repelling moisture, which can retard the decomposition of perovskite film. The device with a SnO_2 buffer layer achieves over 90% of its initial efficiency after 600 h under an ambient condition with relative humidity of 20%–40%. Instead, the control device only exhibits 70% of its initial efficiency. This work provides a facile way of boosting the efficiency and stability of IPSCs, which also gives guidance for perovskite-based tandem solar cells for future commercialization.

Acknowledgements

B.B. Chen and P.Y. Wang contributed equally to this work. The authors gratefully acknowledge the supports from National Key Research and Development Program of China (Grant No. 2018YFB1500103), the Overseas Expertise Introduction Project for Discipline Innovation of Higher Education of China (Grant No. B16027), Tianjin Science and Technology Project (Grant No. 18ZXJMTG00220), and the Fundamental Research Funds for the Central Universities, Nankai University (Grant Nos. 63191736, ZB19500204). Natural Science Foundation of Tianjin (No. 20JCQNJC02070). China Postdoctoral Science Foundation (No. 2020T130317).

Appendix A. Supplementary materials

Supplementary materials to this article can be found online at https://doi.org/10.1088/1674-4926/43/5/052201.

References

[1] https://www.pv-magazine.com/2021/11/22/helmholtz-center-achieves-29-80-efficiency-for-perovskite-silicon-tandem-solar-cell/
[2] Chen B, Ren N, Li Y, et al. Insights into the development of monolithic perovskite/silicon tandem solar cells. Adv Energy Mater, 2021, 2003628
[3] Hou F, Li Y, Yan L, et al. Control perovskite crystals vertical growth for obtaining high-performance monolithic perovskite/silicon heterojunction tandem solar cells with V_{OC} of 1.93 V. Solar RRL, 2021, 5, 2100357
[4] Chen B, Wang P, Li R, et al. Composite electron transport layer for efficient n-i-p type monolithic perovskite/silicon tandem solar cells with high open-circuit voltage. J Energy Chem, 2021, 63, 461
[5] National Renewable Energy Laboratory, Best Research Cell Efficiency Chart. https://www.nrel.gov/pv/cell-efficiency.html
[6] Kim D, Jung H J, Park I J, et al. Efficient, stable silicon tandem cells enabled by anion-engineered wide-bandgap perovskites. Science, 2020, 368, 155
[7] Xu J, Boyd C C, Yu Z J, et al. Triple-halide wide–band gap perovskites with suppressed phase segregation for efficient tandems. Science, 2020, 367, 1097
[8] Zuo C, Ding L. Drop-casting to make efficient perovskite solar cells under high humidity. Angew Chem Int Ed, 2021, 133, 11342
[9] Li F, Deng X, Qi F, et al. Regulating surface termination for efficient inverted perovskite solar cells with greater than 23% efficiency. J Am Chem Soc, 2020, 142, 20134
[10] Unger EL, Kegelmann L, Suchan K, et al. Correction: Roadmap and roadblocks for the band gap tunability of metal halide perovskites. J Mater Chem A, 2017, 5, 15983
[11] Niu G, Li W, Li J, et al. Progress of interface engineering in perovskite solar cells. Sci China Mater, 2016, 59, 728
[12] Xu C, Zhang Z, Hu Y, et al. Printed hole-conductor-free mesoscopic perovskite solar cells with excellent long-term stability using peai as an additive. J Energy Chem, 2018, 27, 764
[13] Lu H, Liu Y, Ahlawat P, et al. Vapor-assisted deposition of highly efficient, stable black-phase $FAPbI_3$ perovskite solar cells. Science, 2020, 370, eabb8985
[14] Min H, Kim M, Lee S U, et al. Efficient, stable solar cells by using inherent bandgap of α-phase formamidinium lead iodide. Science, 2019, 366, 749
[15] Jeon N J, Noh J H, Kim Y C, et al. Solvent engineering for high-performance inorganic-organic hybrid perovskite solar cells. Nat Mater, 2014, 13, 897
[16] Yang W S, Noh J H, Jeon N J. High-performance photovoltaic perovskite layers fabricated through intramolecular exchange. Science, 2015, 348(6240), 1234
[17] Ren Y, Duan B, Xu Y, et al. New insight into solvent engineering technology from evolution of intermediates via one-step spin-coating approach. Sci China Mater, 2017, 60, 392
[18] Zheng X, Hou Y, Bao C, et al. Managing grains and interfaces via ligand anchoring enables 22.3%-efficiency inverted perovskite solar cells. Nat Energy, 2020, 5, 131
[19] Song W, Cao G. Surface-defect passivation through complexation with organic molecules leads to enhanced power conversion efficiency and long term stability of perovskite photovoltaics. Sci China Mater, 2020, 63, 479
[20] Kim M, Kim G H, Lee T K, et al. Methylammonium chloride induces intermediate phase stabilization for efficient perovskite solar cells. Joule, 2019, 3, 2179
[21] Yang X, Fu Y, Su R, et al. Superior carrier lifetimes exceeding 6 micros in polycrystalline halide perovskites. Adv Mater, 2020, 32, e2002585
[22] Yao X, Liang J, Li T, et al. Electron transport layer driven to improve the open-circuit voltage of $CH_3NH_3PbI_3$ planar perovskite

solar cells. Sci China Mater, 2017, 61, 65
[23] Zhu P, Gu S, Luo X, et al. Simultaneous contact and grain-boundary passivation in planar perovskite solar cells using SnO_2-KCl composite electron transport layer. Adv Energy Mater, 2020, 10, 1903083
[24] Wang P, Li R, Chen B, et al. Gradient energy alignment engineering for planar perovskite solar cells with efficiency over 23. Adv Mater, 2020, 32, e1905766
[25] Chen Y, Xu C, Xiong J, et al. Benefits of fullerene/SnO_2 bilayers as electron transport layer for efficient planar perovskite solar cells. Organ Electron, 2018, 58, 294
[26] Wang P, Chen B, Li R, et al. Cobalt chloride hexahydrate assisted in reducing energy loss in perovskite solar cells with record open-circuit voltage of 1.20 V. ACS Energy Lett, 2021, 6, 2121
[27] Liu Z, Krückemeier L, Krogmeier B, et al. Open-circuit voltages exceeding 1.26 V in planar methylammonium lead iodide perovskite solar cells. ACS Energy Lett, 2018, 4, 110
[28] Wu S, Zhang J, Li Z, et al. Modulation of defects and interfaces through alkylammonium interlayer for efficient inverted perovskite solar cells. Joule, 2020, 4, 1248
[29] Xu C Y, Hu W, Wang G, et al. Coordinated optical matching of a texture interface made from demixing blended polymers for high-performance inverted perovskite solar cells. ACS Nano, 2020, 14, 196
[30] Lee J W, Park N G. Chemical approaches for stabilizing perovskite solar cells. Adv Energy Mater, 2019, 10, 1903249
[31] Jia L, Zhang L, Ding L, et al. Using fluorinated and crosslinkable fullerene derivatives to improve the stability of perovskite solar cells. J Semicond, 2021, 42, 120201
[32] Zhang L, Zuo C, Ding L. Efficient $MAPbI_3$ solar cells made via drop-coating at room temperature. J Semicond, 2021, 42, 072201
[33] Ramasamy E, Karthikeyan V, Rameshkumar K, et al. Glass-to-glass encapsulation with ultraviolet light curable epoxy edge sealing for stable perovskite solar cells. Mater Lett, 2019, 250, 51
[34] Matteocci F, Cinà L, Lamanna E, et al. Encapsulation for long-term stability enhancement of perovskite solar cells. Nano Energy, 2016, 30, 162
[35] Zheng H, Dai S, Zhou K, et al. New-type highly stable 2D/3D perovskite materials: the effect of introducing ammonium cation on performance of perovskite solar cells. Sci China Mater, 2019, 62, 508
[36] You J, Meng L, Song TB, et al. Improved air stability of perovskite solar cells via solution-processed metal oxide transport layers. Nat Nanotechnol, 2016, 11, 75
[37] Fang R, Wu S, Chen W, et al. [6, 6]-phenyl-c61-butyric acid methyl ester/cerium oxide bilayer structure as efficient and stable electron transport layer for inverted perovskite solar cells. ACS Nano, 2018, 12, 2403
[38] Liu J, Aydin E, Yin J, et al. 28.2%-efficient, outdoor-stable perovskite/silicon tandem solar cell. Joule, 2021, 5, 1
[39] Köhnen E, Wagner P, Lang F. 27.9% efficient monolithic perovskite/silicon tandem solar cells on industry compatible bottom cells. Sol RRL, 2021, 5, 2100244
[40] Isikgor F, Furlan F, Liu J, et al. Concurrent cationic and anionic perovskite defect passivation enables 27.4% perovskite/silicon tandems with suppression of halide segregation. Joule, 2021, 5, 1566
[41] Zhu Z, Bai Y, Liu X, et al. Enhanced efficiency and stability of inverted perovskite solar cells using highly crystalline SnO_2 nanocrystals as the robust electron-transporting layer. Adv Mater, 2016, 28, 6478
[42] Raninga R D, Jagt R A, Béchu S, et al. Strong performance enhancement in lead-halide perovskite solar cells through rapid, atmospheric deposition of n-type buffer layer oxides. Nano Energy, 2020, 75, 104946
[43] Chen Q, Zhou H, Song T B, et al. Controllable self-induced passivation of hybrid lead iodide perovskites toward high performance solar cells. Nano Letter, 2014, 14, 4158
[44] Cheung S, Cheung N. Extraction of schottky diode parameters from forward current-voltage characteristics. Appl Phys Lett, 1986, 49, 85

Bingbing Chen received her MS degree in Hebei University. She is currently a PhD student under the supervision of Prof. Xiaodan Zhang at Nankai University. Her research interests focus on the development of high-efficiency perovskite/silicon tandem solar cells.

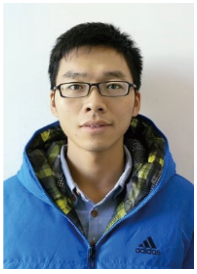

Pengyang Wang received his PhD degree in 2018 at University of Chinese Academy of Sciences (UCAS). Then he joined Xiaodan Zhang group at Nankai University as a postdoc. His research interests focus on efficient and stable metal halide perovskite solar cells and perovskite/silicon tandem solar cells.

Xiaodan Zhang is the professor, doctorial supervisor and director of the Institute of Photoelectronic Thin Film Devices and Technology at Nankai University. Her research interests are mainly in silicon, perovskite and perovskite/silicon tandem solar cells.